Prepared for Biofabrication (2017)

Biofabrication

PAPER

A Heuristic Computational Model of Basic Cellular Processes and Oxygenation during Spheroid-Dependent Biofabrication

T.J. Sego[1], U. Kasacheuski[2,3], D. Hauersperger[2], A. Tovar[1,4], N. I. Moldovan[4,5]

[1] Department of Mechanical Engineering, Indiana University-Purdue University at Indianapolis, IN
[2] Department of Computer and Information Science, Indiana University-Purdue University at Indianapolis, IN
[3] Department of Physics, Indiana University-Purdue University at Indianapolis, IN
[4] Department of Biomedical Engineering, Indiana University-Purdue University at Indianapolis, IN
[5] 3D Bioprinting Core, Indiana University-Purdue University at Indianapolis, IN

Abstract

An emerging approach in biofabrication is the creation of 3D tissue constructs through scaffold-free, cell spheroid-only methods. The basic mechanism in this technology is spheroid fusion, which is driven by the minimization of energy, the same biophysical mechanism that governs spheroid formation. However, other factors such as oxygen and metabolite accessibility within spheroids impact on spheroids properties and on their ability to form larger-scale structures. The goal of our work is to develop a simulation platform eventually capable to predict the conditions that minimize metabolism-related cell loss within spheroids. To describe the behavior and dynamic properties of the cells in response to their neighbors and to transient nutrient concentration fields, we developed a hybrid discrete-continuous heuristic model, combining an Cellular Potts-type approach with field equations applied to a randomly populated spheroid cross-section of prescribed cell-type constituency. This model allows the description of: i) cellular adhesiveness and motility; ii) interactions with concentration fields, including diffusivity and oxygen consumption; and iii) concentration-dependent, stochastic cell dynamics, driven by metabolite-dependent cell death. Our model readily captured the basic steps of spheroid-based biofabrication (as specifically dedicated to scaffold-free bioprinting), including intra-spheroid cell sorting (both in 2D and 3D implementations), spheroid defect closure, and inter-spheroid fusion. Moreover, we found that when hypoxia occurring at the core of the spheroid was set to trigger cell death, this was amplified upon spheroids fusion, but could be mitigated by external oxygen supplementation. In conclusion, optimization and further development of scaffold-free bio-printing techniques could benefit from our computational model able to simultaneously account for both cellular dynamics and metabolism in constructs obtained by scaffold-free biofabrication.

1. Introduction

One of the fundamental properties of cells is their propensity to self-organization. This is essential in all biological processes, from bacterial colony formation to mammalian embryology, organogenesis and tissue repair [1]. Remarkably, although the molecular constituents are encoded in genetic information, there is no genetic “blueprint” for their assembling at any dimensional scale [2]. Supramolecular assemblies are emergent

This is the author's manuscript of the article published in final edited form as:
Sego, T. J., Kasacheuski, U., Hauersperger, D., Tovar, A., & Moldovan, N. I. (2017). A heuristic computational model of basic cellular processes and oxygenation during spheroid-dependent biofabrication. Biofabrication, 9(2), 024104. https://doi.org/10.1088/1758-5090/aa6ed4

structures basically driven by physical principles, such as energy minimization, operating under entropic constraints. For example this explains the round shape of cell clusters, from embryos to tumors [3], also called for this reason cell “spheroids.” Moreover, if there are no additional barriers (such as layers of extracellular matrix) when two such spheroids come in contact, they will fuse and collapse in a larger spheroid [4]. This is possible because within the spheroids the cells perform continuous random movements similar to the Brownian motion of molecules within a liquid droplet [5]. The implications of this similarity hold true for fusing spheroids, such as surface tension [6], contact angle and “neck” diameter [7]. In addition, energy minimization obliges different cells with various adhesiveness to assume an aggregated (often layered) distribution within spheroids [6]. This spontaneous process, called “cell sorting,” is of fundamental importance in embryogenesis and beyond [8].

These phenomena are now exploited for rational design of bio-similar constructs with tissue engineering applications [4, 9], representing the foundation of the emerging “scaffold-free” (i.e., biomaterial-independent) biofabrication. Moreover, cell spheroid fusion either in dual or in larger constructs has been modeled using a variety of methods.

The “building blocks” of biofabrication [10] are either individual cells combined with a supporting matrix (called “scaffolds” [11]) or for increased efficacy, pre-formed clusters of cells [9]. This second approach is indispensable in the scaffold-free versions of biofabrication, where no external materials are used. The goal of producing bio-similar constructs can be attained by using mechanic (such as molding [12]), magnetic [13], or other means. In this case, the constructs solely depend on the extracellular matrix produced by the cells before and during their assembling. Because of biophysical [6] and biological [9] reasons, the clusters usually attain a spherical shape, thus being named cell spheroids. The bio-assembling process is driven by fusion of these spheroids, powered by the same mechanisms which lead to their formation in first place [9].

Spheroid fusion can be also used to voluntarily introduce structural variety, anatomical relevance and scaling-up during biofabrication [14]. These larger-scale constructs often need precise spheroids location for fusion, remodeling and extracellular matrix secretion. Several technologies were considered, some relying on spheroids incorporation into a hydrogel scaffold, followed by their deployment with a bioprinter [15]. However, truly scaffold-free bioprinting methods are preferable, because finding the optimal biomaterial which concurrently satisfies the needs for “bio-inks” and of the embedded cells at the same time can be challenging. But a sufficiently rapid and accurate method to easily combine the spheroids and maintain them for fusion emerged only recently, with the invention of the microneedle array (“Kenzan,” in Japanese) method [16], and subsequent commercialization of the Regenova robot by Cyfuse Biomedical K.K., Japan. Because this instrument basically performs all the operations of a bioprinter, and with the same purpose, it is called a “Bio 3D Printer.” In brief, this consists in lacing the spheroids in contact to each other in a 3D pattern pre-designed by the robot’s computer. Using it, a variety of biological tubes (vascular [16], neural [17], tracheal [18] or ureteral [19]) were “printed,” while other tissues obtained this way are in development.

So far, several computer models of spheroids formation and fusion have been proposed. Depending on the aspect of the process considered these are either more

biomaterial [4], cellular [20] or mixed [21] orientation. However, due to severe computational limitations, these methods took into consideration neither intracellular (e.g., metabolism) nor extracellular (e.g., chemotactic) aspects of their environment which depend on continuous, diffusive processes.

In this study, we present a computer model that incorporates both cellular-level (discrete) and molecular-level (continuous) phenomena. This model thus represents a "hybrid" treatment of the basic steps in scaffold-free biofabrication. We accomplish this by relating physical characteristics and processes to the Cellular Potts model (CPM) [22], a discrete, lattice-based kinetic Monte Carlo (KMC) method known to reproduce dynamical properties and morphological phenomena by considering events at the cellular level [23]. While other models like Cellular Particle Dynamics (CPD) [21], Lattice Boltzmann (LB)[24] methods, and phase field theory [4] have been shown to also predict certain characteristics of bioprinting, we selected the CPM for its well-established ability to capture emergent cell dynamics, such as cell sorting and spheroid fusion [23], its treatment of cells as , and for the simplicity of its formulation, which we intend to extend in future work.

Although both the CPM and diffusion modeling have been previously formulated in both two-dimensional and three-dimensional space [25, 26], we first investigated the usefulness of our hybrid treatment of the simulation in a simpler, more readily accessible qualitative way (i.e., by 'heuristic modeling').

Materiality in the CPM is accomplished by treatment of the discrete domain similar to the discretization of continuous domains in common numerical methods like the finite difference and the finite element methods. To this end, we model cells with physical attributes like nominal spatial occupancy and metabolic rates, and the domain as having physical dimensions, chemical species and diffusion coefficients. We map these characteristics onto the discrete domain of the CPM, and conversely map the effects of the population in the discrete domain onto expressions of mass diffusion as reaction-diffusion systems [27]. We then simulate metabolic activities during morphological phenomena and corresponding cell death due to the formation of hypoxic regions.

2. The Model

The modeling of cellular dynamics was formulated according to the CPM [22] and implemented in two dimensions in MATLAB R15a. The model consists of a regular, discretized d-dimensional lattice $\mathcal{L}$ of a medium populated by cells. For both the medium and all cells, henceforth collectively referred to as agents, each agent i is initialized with a unique identification number $\sigma_i \in \mathcal{I}$ such that those lattice sites occupied by agent i are denoted with the corresponding value $\sigma(r,k) = \sigma_i$, where $r \in \mathcal{L}$ and k is the virtual time. $\mathcal{L}$ is mapped to a physical, continuous domain $\mathcal{P}$ by a modeling coefficient $\alpha : \mathcal{L} \to \mathcal{P}$ such that $x = \alpha r \in \mathcal{P}$ is a physical coordinate and $\alpha^d|\mathcal{L}|$ is the physical d-dimensional space that corresponds to $\mathcal{L}$.

Every agent was modeled with a set of modeling descriptors according to its type $\tau = \tau(\sigma)$, where two cells of the same type are modeled identically. Implementation of the

model handles an arbitrary number of agents and agent types, where the medium is always simulated with an integer values of zero for cell identification and type.

The modeling of a concentration field $C = C(x,t)$ is performed by a parabolic differential equation,

$$\partial_t C = D\partial_{ii} C + S, \qquad (1)$$

where all agents are assumed to have the same diffusion coefficient D, $S = S(x,t)$ is a source field and $t = \beta k$ is the physical time related to simulation step k by the modeling coefficient β, which represents the time calibration (currently being in progress). Implementation of the model permits an arbitrary number of independent concentration fields and solves each diffusion system using second-order central difference scheme, forward Euler explicit integration, and Dirichlet boundary conditions with a prescribed boundary value C_0.

2.1. Cellular Dynamics

Cell motility is simulated by considering a set of randomly selected copy attempts, called a Monte Carlo step (MCS). For each copy attempt in a MCS, a source site $r^s \in \mathcal{L}$ and target site $r^t \in \mathcal{N}(r^s)$ in the von Neumann neighborhood of range one $\mathcal{N} \subseteq \mathcal{L}$ of the source site are both randomly selected. For all performed simulations, the number of copy attempts per MCS was equal to the number of lattice sites, though implementation permits an arbitrary specification of copy attempts per MCS. For MCS k, if the copy attempt is accepted then, at virtual time $k + \Delta k$ after the copy attempt (i.e., $|\mathcal{L}|\Delta k = 1$), $\sigma(r^t, k + \Delta k) = \sigma(r^s, k)$. The probability of each copy attempt is considered as the stochastic rule

$$P\big(\sigma(r^t, k + \Delta k) = \sigma(r^s, k)\big) = e^{-\max\left\{0, \frac{\Delta\mathcal{H}}{\mathcal{H}^*}\right\}}, \qquad (2)$$

where $\Delta\mathcal{H}$ is the change in the system Hamiltonian $\mathcal{H}$ due to the copy attempt. The system temperature $\mathcal{H}^* \in \mathbb{R}_+$ is a modeling coefficient. In this way, copy attempts are accepted such that the system energy tends to decrease, where the likelihood of an increase in energy is inversely proportional to the magnitude of the increase.

We denote here the definition of $\mathcal{H}$ as a summation of independent Hamiltonians $\mathcal{H}^i$ that pertain to the modeling of various cellular phenomena,

$$\mathcal{H} = \sum_i \mathcal{H}^i. \qquad (3)$$

A spatial constraint $v_c^\tau \in \mathbb{R}_+$ is imposed on each cell by the Hamiltonian $\mathcal{H}^v$ such that the number of lattice sites $|\mathcal{V}^{\sigma_i}|$ in the subdomain $\mathcal{V}^{\sigma_i} \subseteq \mathcal{L}$ occupied by cell σ_i tends toward $v^{\tau(\sigma_i)}$, satisfying

$$\mathcal{H}^v = \sum_{i=1}^{|\mathcal{I}|} \lambda_v^{\tau(\sigma_i)} \left(|\mathcal{V}^{\sigma_i}| - v^{\tau(\sigma_i)} \right)^2, \qquad (4)$$

where the geometric Lagrange multiplier $\lambda_v^\tau \in \mathbb{R}_+$ is a modeling coefficient for the cell type τ.

Contact energy is modelled at each agent-agent interface by the Hamiltonian $\mathcal{H}^h$,

$$\mathcal{H}^h = \sum_{i=1}^{|\mathcal{L}|} \sum_{j=1}^{|\mathcal{M}(r^i,k)|} \left(1 - \delta_{\sigma(r^i,k),\sigma(r^{j,i},k)}\right) J\left(\tau\left(\sigma\left(r^i,k\right)\right), \tau\left(\sigma\left(r^{j,i},k\right)\right)\right), \qquad (5)$$

where $\delta_{p,q}$ is the Kronecker-delta, $\mathcal{M}\left(r^i,k\right)$ is the Moore neighborhood of range one of $r^i \in \mathcal{L}$, $r^{j,i} \in \mathcal{M}\left(r^i,k\right) \subseteq \mathcal{L}$ is the j^{th} neighbor of r^i and the contact energy $J(\tau,\tau') = J(\tau',\tau) \in \mathbb{R}_+$ between the agent types τ and τ' is a modeling coefficient of the two types. Implementation of the model also permits the modeling of $\mathcal{M}$ as a Moore neighborhood of range two, and as a von Neumann neighborhood of ranges one and two.

The chemotaxis modeling is performed by the Hamiltonian $\mathcal{H}^c$,

$$\mathcal{H}^c = \sum_{i=1}^{|\mathcal{L}|} \lambda_c^{\tau\left(\sigma\left(r^i,k\right)\right)} C\left(\alpha r^i, \beta k\right), \qquad (6)$$

where the chemotactic Lagrange multiplier $\lambda_c^\tau \in \mathbb{R}$ is a modeling coefficient for the cell type τ. For all simulations that did not consider chemotaxis, $\mathcal{H} = \mathcal{H}^v + \mathcal{H}^h$, and for simulations that considered chemotaxis, $\mathcal{H} = \mathcal{H}^v + \mathcal{H}^h + \mathcal{H}^c$.

2.2. Additional Cell-Environment Interactions

The source field S is related to the agent type found at r in $\mathcal{L}$ that corresponds to x in $\mathcal{P}$. This is

$$S(x,t) = \frac{s^{\tau\left(\sigma\left(\alpha^{-1}x,\beta^{-1}t\right)\right)}}{\left|\mathcal{V}^{\tau\left(\sigma\left(\alpha^{-1}x,\beta^{-1}t\right)\right)}\right|\left(v^{\tau\left(\sigma\left(\alpha^{-1}x,\beta^{-1}t\right)\right)}\right)^{3d^{-1}}}, \qquad (7)$$

where the molar consumption rate s^τ is a modeling coefficient of cell type τ. Each cell type τ is modeled with a corresponding dead type $\tau^d = \tau^d(\tau)$ such that all modeling coefficients are the same except

$$\begin{aligned} v^{\tau^d(\tau)} &= \frac{v^\tau}{4}, \\ s^{\tau^d} &= 0. \end{aligned} \qquad (8)$$

The phenotypic response of hypoxic cell death is modeled as a stochastic function of the mean concentration field $C^{\sigma_i}(t)$ in the subdomain $\mathcal{X}^{\sigma_i} \subseteq \mathcal{P}$ of cell σ_i (i.e., $\mathcal{X}^{\sigma_i} = \alpha\mathcal{V}^{\sigma_i}$),

$$C^{\sigma_i}(t) = \frac{1}{\alpha^3 |\mathcal{V}^{\sigma_i}|} \int_{\mathcal{X}^{\sigma_i}} C(x,t)dx. \qquad (9)$$

The probability of cell death is then considered once every MCS for each cell according to a normal distribution,

$$\begin{aligned} &P\left(\tau\big(\sigma(r,k+1)\big)\right. \\ &\left.= \tau^d\left(\tau\big(\sigma(r,k)\big)\right)\right) \\ &= \beta p^{\tau(\sigma(r,k))} e^{-\left(\frac{C^{\sigma(r,k)}(\beta k)}{\gamma^{\tau(\sigma(r,k))}}\right)^2}, \end{aligned} \qquad (10)$$

where the probability rate p^τ and standard deviation γ^τ are modeling coefficients for the cell type τ. All stochastic state changes are implemented by the following general routine: 1) calculate the probability of the occurrence of the state change; 2) draw a random variable in [0, 1]; and 3) the state change occurs if the random variable is less than or equal to the probability, otherwise the state is unchanged.

3. Results

Simulations were performed to demonstrate various emergent phenomena of the model described in Section 2. All cell types were assumed to have the same geometric constraint and Lagrange multipliers, and cell types were modeled as human induced pluripotent stem cells (iPSCs) and iPSC-derived neurons [26]. Unless otherwise specified, the modeling coefficients of Table 1 were used for all relevant simulations. All CPM coefficients were taken from Graner [22], except for the contact coefficient between high-adhesion cells ($J(1,1)$), which was modified to reduce excessive deformation of those cells. The discretization length was selected such that for an initial square cell geometry, a seven-by-seven square in the lattice is approximately equal to the geometric constraint of the cell. We chose this due to that spheroids in all simulations were initialized with square-shaped cells, and that initializing cells nearer to their geometric constraint reduces initialization artifacts like immediate spheroid expansion or contraction. Coarser resolutions (e.g., to produce a four-by-four square cell) demonstrated simulation artifacts in both the discrete and continuous domains, particularly concerning convergence of diffusion solutions, while a resolution to produce an eight-by-eight square cell presented excessive computational cost without contributing any noticeable additional accuracy. The time correlation was arbitrarily chosen to produce demonstrative results of our hybridization. The medium is shown as blue, iPSCs as yellow and neurons as brown. The medium, iPSCs and neurons were assigned the agent-type integer values zero, one and two, respectively.

Table 1. Modeling coefficients used for all simulations (unless otherwise specified).

Coefficient	Symbol	Value
System temperature[c]	$\mathcal{H}^*$	10
Geometric constraint[a]	v^τ	43.5 μm^2
Discretization length	α	942 nm
Time correlation (in 2D)	β	0.1 s/MCS
Diffusion coefficient[b]	D	2,500 μm^2/s
Geometric Lagrange multiplier[c]	λ_v^τ	1
Contact energy coefficients[c]	$J(0,0)$	0
	$J(0,1)$	16
	$J(0,2)$	16
	$J(1,1)$	6
	$J(1,2)$	11
	$J(2,2)$	14
Consumption rates (mol/cell/s)[b]	s^1	-1.8×10^{-18}
	s^2	-7.7×10^{-16}

[a]Wakao, 2012 [28]
[b]McMurtrey, 2016 [26]
[c]Graner, 1992 [22]

3.1. Cell Sorting

First, we verified if our program can capture the key features of this modeling class, namely cell sorting [8] and spheroids fusion [29]. Together, these features are needed to validate the program in comparison with the current approaches using similar methods, such as CompuCell 3D (CC3D) [30], KMC methods, or CPD [21]. Because the oxygen diffusion equations within spheroids were taken from a study calibrated for induced pluripotent stem cells cerebral organoids, supposedly not all differentiated simultaneously, we assumed that generic cell spheroids would contain a mixture of such more primitive and adhesive (considered as iPSC), and more adult (considered as neural) cells.

We found that, indeed, the phenotypic layering known as “cell sorting” readily emerged in spheroids composed of two cell types with different intercellular adhesiveness (Figure 1). This result is consistent with empirical observations [6] and with CPM predictions [31]. We also observed that for all cell proportions, a perimeter of low-adhesion cells emerged by the end of simulation, the formation of which was observed to begin with those low-adhesion cells initialized nearest to the perimeter. Clusters of low-adhesion cells aggregated very early throughout each spheroid and combined by random motion. The perimeter was further populated by those aggregates of low-adhesion cells that happened to come into contact with the perimeter, since no mechanisms besides

differential adhesion were considered to direct cell motility. This explains the observed final configuration of some spheroids with isolated aggregates ("islands") of low-adhesion cells: a lower concentration of low-adhesion cells increases the likelihood of their aggregates at the core to be surrounded by a region of high-adhesion cells. Escape of cells from such islands is contingent of a number of factors which were beyond the scope of our study. Similar observations were made in the 3D implementation of the model (below).

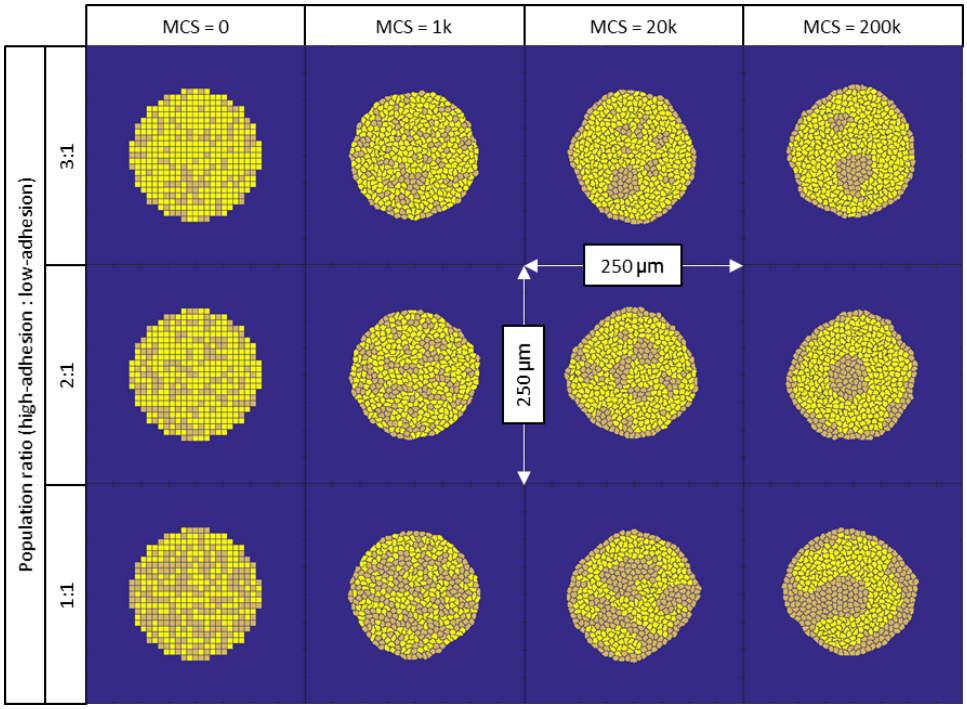

Figure 1. Simulation of cell sorting process within spheroids. Spontaneous cell layering in a binary cell-type spheroid (iPSCs are yellow and neurons are brown), based on the strength of their interaction, for various cellular proportions. Note the isolated inner region ("island") of low-adhesion cells for the greater proportions of high-adhesion cells.

3.2. Spheroids fusion

We then reproduced the phenomenon of spheroid fusion [14], both with single-cell spheroids (not shown), or using heterogeneous spheroids of varying cellular proportions (Figure 2). In this case, we also analyzed how spheroid fusion interferes with cell sorting (Figure 2A). This occurs as the emerging, single spheroid expands, which creates a greater distance from the perimeter for isolated, low-adhesion aggregates near the emerging core. In practice, this may highlight occult structural inhomogeneity within fusing spheroids [32]. Quantification of fusion was performed by tracking the aspect ratio of the construct, which was calculated as the ratio of the neck diameter [7] along the vertical dimension to the major diameter along the horizontal dimension (Figure 2B). From this, we also found that cell composition has a sizable effect on the rate of fusion, which increases with the proportion of stronger interacting cells (Figure 2C). This is readily explained by the effects of adhesion properties at the cellular level, where from

more high-adhesion intercellular interactions emerges a macroscopic increase in the rate of fusion.

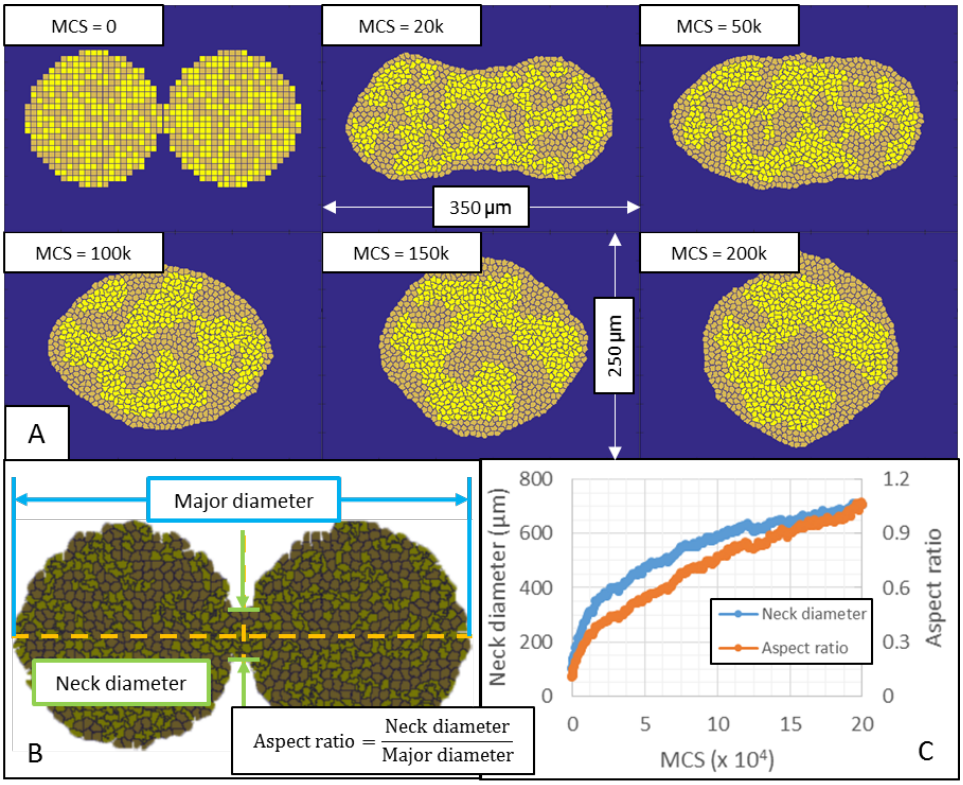

Figure 2. Modeling of spheroid fusion. A. Simulation of spheroids fusion with concurrent cell sorting (iPSCs are yellow and neurons are brown). **B**. How the aspect ratio and neck dimeter were defined. **C**. Tracking spheroid fusion by measuring neck diameter and aspect ratio vs. virtual time.

3.3. Self-healing of spheroid defects

Related to spheroids formation, and driven by the same mechanism, is the eventual closure of any defects ("holes") in the spheroids. This self-healing is particularly relevant for the Kenzan method of 3D biofabrication, where the spheroids are temporarily held in microneedles as supports for their fusion and post-printing maturation [32]. After extraction from the needles, in the spheroids are left hollow cylindrical holes of a needle's size, which were shown to be quickly resorbed [16]. This has been assumed to happen due to the same energy minimization process [33] and, in the absence of cell division, with a similar kinetics as during cluster rounding and spheroid fusion. Thus, for prediction and optimization purposes we also modeled this process in 150 micrometer diameter spheroids (Figure 3). We simulated the closure of a round defect as dependent on the strength of intercellular adhesions by varying the binary cellular composition (Figure 3A). Increasing the proportion of cells with higher adhesiveness generally lead to a faster hole closure, which was calculated as the initial hole area divided by the simulation time required for closure (Figure 3B). A linear curve was also well fit to the area of the hole vs. virtual time for one trial each cellular composition (Figure 3C). Results showed extreme rates for homogeneous spheroids, where the fastest closure rate occurred for high-adhesion cells, and the lowest for low-adhesion cells. Closure rates for

intermediate cellular compositions decrease with increasing low-adhesion cell concentration in a nonlinear manner.

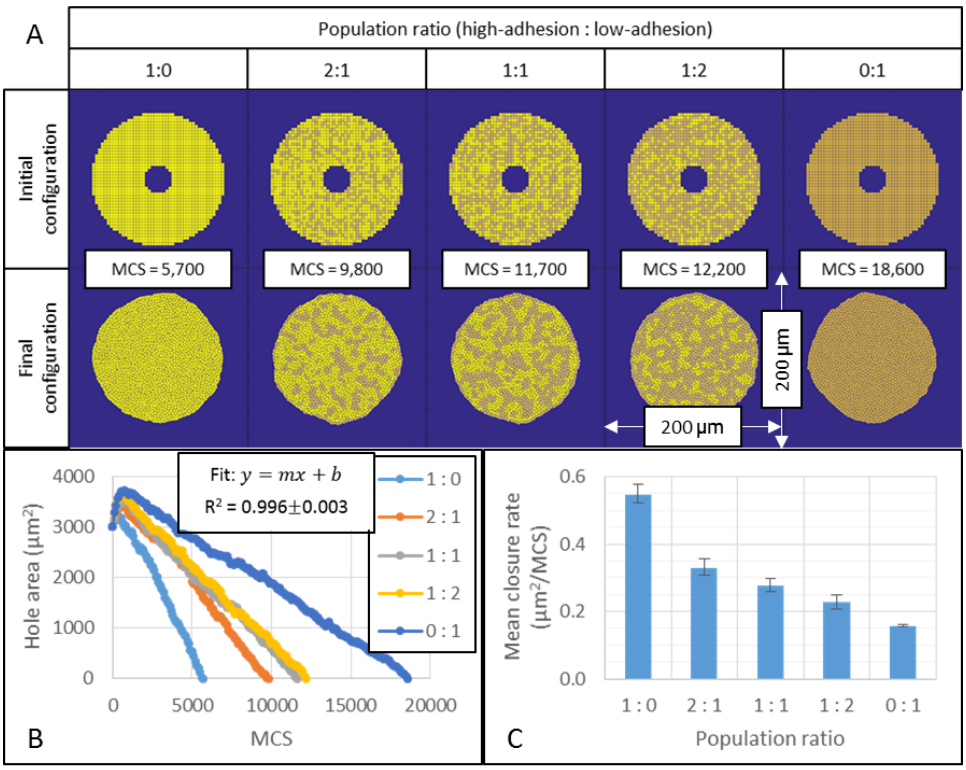

Figure 3. Defect self-healing in heterogeneous spheroids. A. Spheroid configuration immediately after hole closure (same color code as in Fig. 2). Note the decrease in time to closure with increasing ratios of high-adhesion cells. **B**. Kinetics of hole closure as dependent on cell composition. C. Mean hole closure rate calculated from all trials of each cell concentration. Error bars demonstrate the variance in each set of trials.

3.4. Oxygen diffusion

The main purpose to develop our hybrid method was to move beyond spheroid simulations performed so far, which mainly consider adhesion and random motion, by also taking into consideration their cellular metabolism and survival. To begin with, we implemented the diffusion and consumption of oxygen within spheroids made from iPSCs and neurons, similarly to McMurtrey [26] . Unlike this previous work, the introduction of a diffusion system to the Cellular Potts model permits the study of spheroid metabolism due to individual cell consumption while also taking into consideration intra-spheroid cell mobility. Then, the hybrid model was applied to spheroids of various size, number and cellular consistency while considering cell survival.

First, we analyzed cells with identical intercellular interactions, but with different rates of oxygen consumption, under steady-state conditions (Figure 4A). When the cell population in each of two fusing spheroids was randomly distributed, the distribution of oxygen was approximately symmetrical, whereas uniformly distributed initial populations exhibited. As expected, each fusion simulation produced a single, randomly

distributed spheroid with indistinguishable oxygen distributions. We then simulated partial fusion of two spheroids of 250 micrometers in diameter considering differential adhesion (

Figure 4B). Results showed the development of greater oxygen depletion at the fusion interface of the spheroids as fusion occurred, demonstrating that cells at the core of the resulting fused structure experience more severe hypoxia. Concentration values in the emergent, single spheroid were observed to be qualitatively consistent with both theoretical predictions and measured values *in vitro* [26, 34, 35]. We then expect that our hybridization of the CPM produces reliable predictions about the environmental effects of metabolic activities in the simulation space, with particular relevance concerning the development of hypoxic regions during morphological phenomena like spheroid fusion.

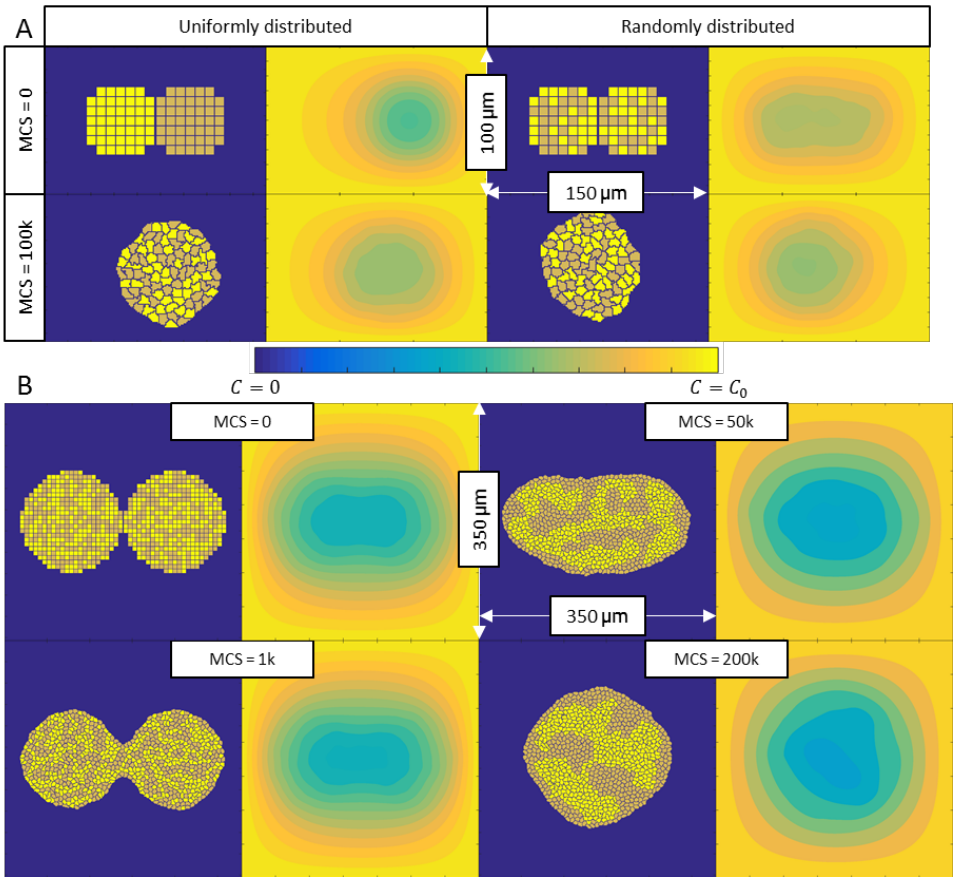

Figure 4. Oxygen redistribution during spheroid fusion under steady-state conditions. A. Fusion of 50 micron-diameter spheroids for different initial cell distributions, with cells of identical adhesive but different metabolic properties ($\boldsymbol{C_0} = 0.02$ mM, $\boldsymbol{J(1,1) = J(1,2) = J(2,2) = 6}$). Besides diffusion, cell mixing also contribute to oxygen concertation uniformization across the fused structure. **B**. Oxygen concentrations during fusion of heterogeneous, 150 micron-diameter cell spheroids ($\boldsymbol{C_0} = 0.22$ mM). Note the development of greater oxygen depletion in the emerging fused structure.

3.5. Coupling oxygenation and cell death

Meaningful results were also obtained after coupling spheroid oxygenation and cell survival (Figure 5). For computational reasons, a uniform spheroid of neurons was

initiated with a diameter of 150 microns and simulated in a hypothetical 0.16 mM environmental oxygen. Cell death was implemented as described in Section 2.2.

In this experiment, we examined two temporal ranges of the same simulation: one is the early development of the concentration gradient and onset of hypoxia, and the other is the long-term effects after severe depletion of oxygen. In the early phase, the reduction of available oxygen was naturally associated with cell loss and the development of a transient necrotic core (Figure 5A), consistently with *in vitro* results [36, 37]. However, in the last phase with massive cell death there was a rebounding of oxygenation (Figure 5B), due to both decreased total cell consumption and to spheroid shrinkage (given that the size of dying cells was set to decrease with 50%). This was observed in the notable lack of a concentration gradient at the center of the domain with further development of the necrotic core, which measured consistently with *in vitro* work that demonstrate the interactions of diffusive nutrients and cell viability in spheroidal aggregates [34, 35].

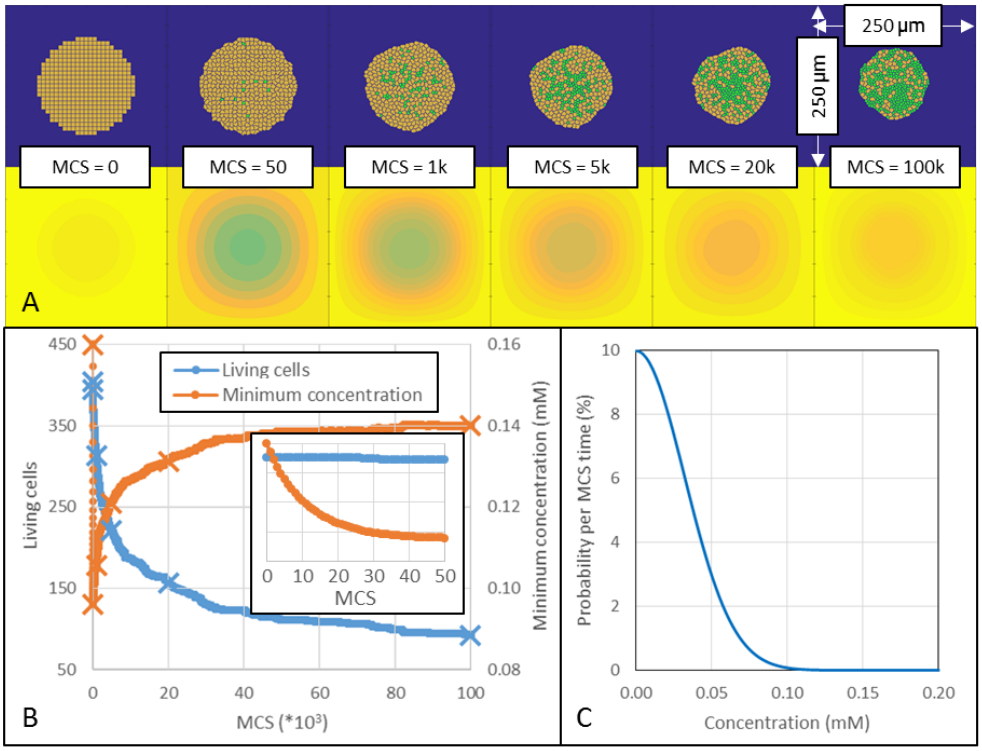

Figure 5. Simulation of cell survival kinetics in a 150 micron-diameter spheroid as dependent on O_2 concentration ($C_0 = 0.16$ mM). **A**. Progressive hypoxia and mild cell loss developing as an effect of spheroid metabolism (living neurons are brown, dead neurons are green). **B**. In the insert, interaction of living cell population (blue) and minimum value of oxygen distribution (orange). Note the decreasing rate of cell death and recovery of oxygen in the main figure. **C**. Dependence of cell death probability per MCS on oxygen concentration.

3.6. Impact of hypoxia on cell survival in biofabricated constructs

Equally relevant for biofabrication is to know the impact of size and shape of a construct and corresponding metabolism on hypoxia-related cell survival. We simulated these here by comparing the oxygen distribution and related cell death in one, two and four fusing spheroids (each of an initial diameter of 50 micrometers) (Figure 6). The probability of cell death was modeled with the curve in Figure 5C ($\beta p^{\tau} = 0.1$, $\gamma^{\tau} =$

0.045 mM). We found that cell death is proportional to initial construct size (Figure 6A, C), but this can be mitigated by increasing environmental oxygen (Figure 6B, C).

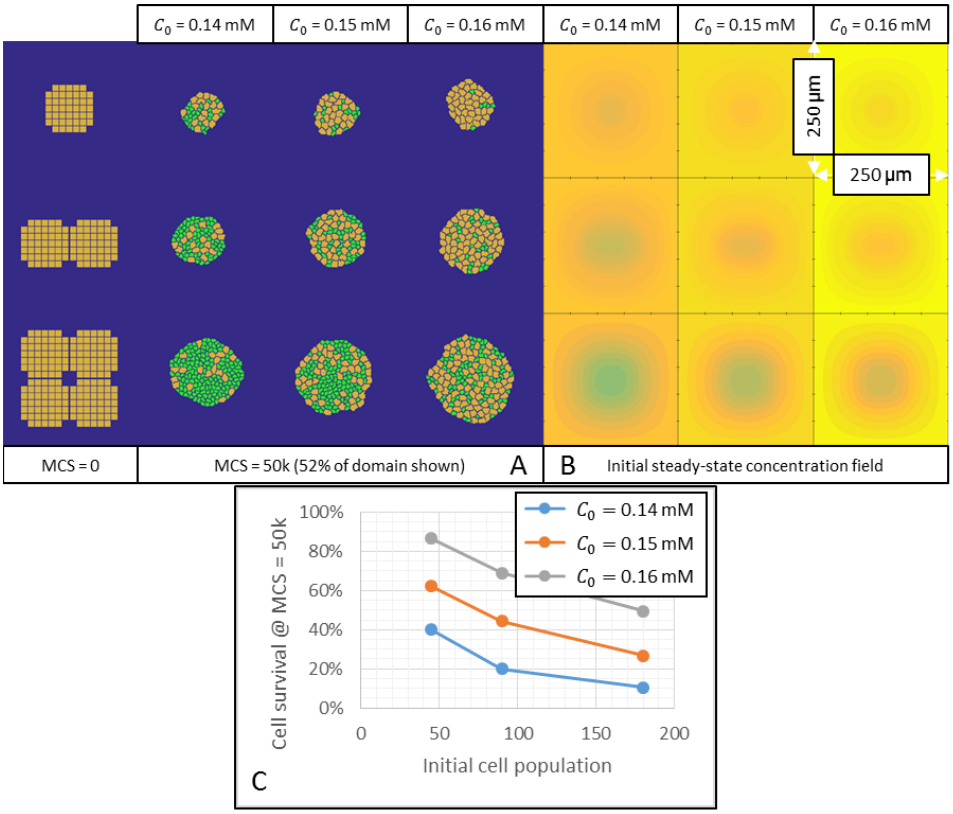

Figure 6. Impact of hypoxia on cell survival of various constructs. A. Construct initial and final configurations for three concentration boundary values (living neurons are brown, dead neurons are green. 52% of the cellular domain shown). Cell death was modeled with the curve in Figure 5C. **B.** Steady-state concentration field of initial configuration for all trials. **C**. Dependence of cell survival on construct's initial size (number of cells) and on ambient oxygen concentration. Note the rescuing effect of environmental oxygen on cell survival, explaining the benefit of fresh medium perfusion in Kenzan technology.

3.7. Expansion of the model to the third dimension

The two-dimensional implementation of the model provided a faster testing of its capabilities and heuristic insights, but its refinement and some of the actual applications require the three-dimensional implementation. This is exemplified by the process of cell sorting [8] and shown in Figure 7. Expectedly, the time to perform one MCS step has increased about 40 times for a comparable discretization length of 1.2 µm. However, the actual cell distribution recapitulates that in the two-dimensional case (Figure 1).

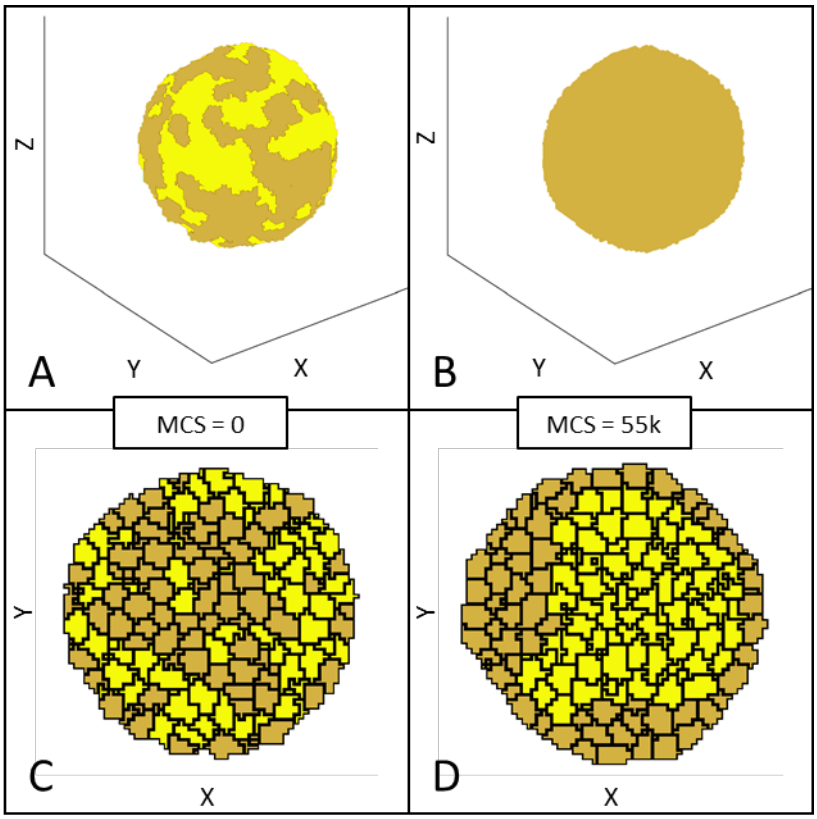

Figure 7. Cell sorting in a 3D version of the model. A. 3D view of a mixed spheroid (cell proportions were 1:1), at the beginning of simulation. **B**. 3D view of the final configuration at the end of simulation (55,000 MCS). **C**. Cross-sectional view of the initial, randomly populated configuration in the XY-plane. **D**. Cross-sectional view of the final, sorted configuration in the XY-plane.

4. Discussion

In this study we demonstrate a model capable to capture the essential features and behavior of cell spheroids as used in scaffold-free biofabrication, similar to other methods developed for this purpose, such as CC3D [30], KMC or CPD [21]. However, our model goes beyond them by incorporating the coupling of diffusive oxygen metabolism and oxygen-dependent stochastic cell death [38]. Another advance is that, unlike the previous methods, for every simulated phenomenon we considered two cell populations (and more can be easily added), to more realistically account for biofabrication practice.

While acknowledging the fundamental importance of an accurate 3D model, there were three reasons to start with this simpler 2D version: a) the computational time is much longer in 3D than in 2D; b) for the creation of a 'hybrid' with the CPM, our focus was more on the implementation of the diffusional field; c) in some applications, such as cell sorting, the 2D and 3D versions produce similar results, as shown here as well.

We applied our model to the basic steps of scaffold-free, microneedle-based bioprinting method, where pierced multicellular spheroids are brought in contact to fuse and thus generate 3D constructs [32]. Since after removal from the needles, holes in the spheroids need to "heal", we simulated this process and found that its rate of completion

indeed depends on the cellular composition of the spheroid. The rate of closure of a cylindrical defect was found to be significantly affected by the ratio of high- to low-adhesion cells, and behave in a nonlinear manner. Homogeneous high- and low-adhesion cell populations produced the fastest and slowest rates, respectively, with intermediate mixed populations decreasing the closure rate in a nonlinear manner with increasing number of low-adhesion cell. Future work simulating more trials and more cellular compositions could be performed in conjunction with experimental work to confirm this observation, and to investigate the extent to which cell sorting affects closure. To this end, simulations could also be performed that compare the rate of closure for spheroids that are initialized with sorted and randomly distributed cellular configurations.

Hypoxia, often combined with nutrient depletion and/or waste accumulation, collectively called "ischemia", is a key factor in determining cell survival and functioning in compact cell aggregates [39]. It is known that oxygen is consumed *in vivo* within about 200 microns distance, unless a blood supply is provided [40]. But the diameter of cell spheroids used for Kenzan bioprinting (which takes hours to perform and days to mature [32], may surpass twice this distance, making the core of spheroids necessarily hypoxic.

To implement a continuous oxygen diffusion and consumption in spheroids, we pursued ideas from a published model using human induced pluripotent stem cells-derived neurons [26]. This was performed in our model by coupling oxygen concentration with cell survival using a distribution function to model the likelihood of cell death as dependent on local hypoxia. In conditions of substantial cell loss, we found that oxygen levels may rebound, due to both the diminished number of individual consumers and the emergent shrinkage of the spheroid. In fact, this effect was observed experimentally in our previous study of oxygen distribution in the mouse heart after experimental myocardial infarction [41]. Overall, this is a very good illustration of emergent phenomena taking place in ensembles such as cell spheroids, which are efficiently captured by agent-based modeling simulations.

From a practical perspective, it is also important to know what happens when spheroid fusion is scaled-up to larger constructs. In the absence of a microcirculation, oxygen diffusion will naturally be even more impaired in multi-spheroid constructs, thus proportionally increasing cell death. Encouragingly however, the system seems to remain very sensitive to the boundary (environmental) oxygen concentrations. This suggests the exposure to supra-physiological oxygen ('hyperbaric oxygen' [42]) as a means to mitigate the detrimental effects of hypoxia in bio-fabricated constructs. Future modeling work could also be performed using Neumann boundary conditions in the implementation of diffusion systems, for predictive capabilities concerning controlled perfusion during biofabrication.

The main advantage of our model comparing to others developed so far is the combination of conceptual realism with simplicity and operability. For example, the coincident effects of cell mixing, cell death and oxygen diffusion could be simulated in a structure complicated enough (i.e., four fusing spheroids), to be meaningful for better understanding a basic step in biofabrication. Moreover, our model has these additional features: a) puts the emphasis on the analysis of metabolism; b) develops a novel formalism for phenotypic response to environment; c) provides the proof of concept of

hybridization, opened to further improvement; d) has similar, or even lower computational cost to other KMC methods; e) although CPM like CPD and LB methods are not well suited for parallelization, the hybridization makes ours acceptable for parallel computation of stochastic functional response and diffusion. Among the main limitations, we mention the lack of temporal calibration (work in progress), as well modest computational efficiency (due to the use of MATLAB).

Looking ahead for the potential of our model to address other important questions in this form of biofabrication after this stage of development, our model is capable of refinements and extensions. For example, we will study the effect of microneedle puncture on oxygen distribution and cell survival in spheroids. We anticipate that the hole created by the needle could be in fact beneficial for overall construct viability, by creating another diffusive interface with the environment. Moreover, when comparing fusion between intact spheroids and those immobilized in the needles, the latter may present an increased efficiency, since the needle occupies some of the region where hypoxic cell death is expected to occur.

But firstly, and mostly needed, is to proceed with the implementation in 3D domain. Other extensions will involve the improvement of simulating diffusion systems and coupled cellular activities. One example is the implementation of chemotactic fields, with the concentration gradient acting as a chemoattractant that facilitates directional cell migration as shown in Equation (6). Within the spheroids, this field may overcome the passive cell sorting mechanism of cell positioning. If the cells are of vascular nature, this chemoattractant could be the vascular endothelial growth factor, with a secretion triggered by hypoxia and with a distribution inversely mirroring of that of oxygen in the spheroids [43]. To simulate this effect, we plan to add concentration field interactivity, allowing, for example, the crosstalk of oxygenation and cell signaling, and their impact on cell survival and migration.

The model could be even further refined by incorporating other metabolites, such as glucose generation and lactate production, each with their separate yet cumulative effects on cell survival and mobility. With the simulation of additional chemical species, our model may then be relevant for the simulation of other cellular responses, such as cell division and differentiation, both of which have already been added in our implementation using an expression similar to Equation (10). For modeling of biofabrication methods with controlled perfusion, or alter blood flow in tissue engineered constructs *in vivo*, we will also add functionality to simulate the Neumann and mixed boundary conditions.

Finally, our model, which is now spatially calibrated, needs to be temporally calibrated as well. This could be accomplished in several alternative yet complementary ways, using different correlation methods like the duration of a complete spheroid fusion and/or its sensitivity to cell proportions, kinetics of intra-spheroid cellular migration, time or rate of hole closure, etc. The relating of physical and virtual time is particularly relevant to our future work concerning chemical species, since diffusion systems necessarily introduce physical time to simulation. Accomplishing this time correlation, we can then work to calibrate the parameters used to model hypoxic cell death probability

as well as additional chemical-dependent cellular responses according to experimental evidence.

5. Conclusions

Hybrid models of cell spheroids hold the potential of optimization of scaffold-free biofabrication. In particular, CPM describes well the dynamics of cell spheroids fusion during scaffold-free biofabrication. Incorporation of oxygen metabolism in the models shows how it may control the outcome of biofabrication. While expectedly the construct size has a proportional effect on oxygen distribution, using our model we found that the spheroids show high, sometimes counter-intuitive sensitivity to metabolic and environmental O_2. This suggested that the 'treatment' with hyperbaric oxygen of cell constructs could be beneficial for improving the efficiency of biofabrication. This model will be improved by completing its 3D implementation, calibration, and expansion to include other aspects of cell metabolism.

6. Acknowledgements

The authors are grateful to Drs. P. Macklin and A. Neagu for critical reading of the manuscript. This work was made possible by support from the Department of Mechanical Engineering of IUPUI School of Engineering and Technology, and by a MURI grant from the Center of Research and Learning at IUPUI. The 3DBP Core facility received support from the Offices of Executive Associate Dean of Research, Indiana University School of Medicine (IUSM), and of Vice Chancellor for Research at Indiana University-Purdue University at Indianapolis (IUPUI).

References

1. Neagu, A., et al., *Role of physical mechanisms in biological self-organization.* Physical review letters, 2005. **95**(17): p. 178104.
2. Swat, M.H., et al., *Multi-scale modeling of tissues using CompuCell3D.* Methods in cell biology, 2012. **110**: p. 325.
3. Shirinifard, A., et al., *3D multi-cell simulation of tumor growth and angiogenesis.* PloS one, 2009. **4**(10): p. e7190.
4. Yang, X., V. Mironov, and Q. Wang, *Modeling fusion of cellular aggregates in biofabrication using phase field theories.* Journal of theoretical biology, 2012. **303**: p. 110-118.
5. Mombach, J.C. and J.A. Glazier, *Single cell motion in aggregates of embryonic cells.* Physical review letters, 1996. **76**(16): p. 3032.
6. Beysens, D., G. Forgacs, and J. Glazier, *Cell sorting is analogous to phase ordering in fluids.* Proceedings of the National Academy of Sciences, 2000. **97**(17): p. 9467-9471.
7. McCune, M., et al., *Predictive modeling of post bioprinting structure formation.* Soft matter, 2014. **10**(11): p. 1790-1800.
8. Zhang, Y., et al., *Computer simulations of cell sorting due to differential adhesion.* PloS one, 2011. **6**(10): p. e24999.
9. Mironov, V., et al., *Organ printing: tissue spheroids as building blocks.* Biomaterials, 2009. **30**(12): p. 2164-2174.
10. Groll, J., et al., *Biofabrication: reappraising the definition of an evolving field.* Biofabrication, 2016. **8**(1): p. 013001.
11. Kang, H.-W., J.J. Yoo, and A. Atala, *Bioprinted scaffolds for cartilage tissue engineering.* Cartilage Tissue Engineering: Methods and Protocols, 2015: p. 161-169.
12. Murata, D., et al., *A preliminary study of osteochondral regeneration using a scaffold-free three-dimensional construct of porcine adipose tissue-derived mesenchymal stem cells.* Journal of orthopaedic surgery and research, 2015. **10**(1): p. 35.
13. Souza, G.R., et al., *Three-dimensional tissue culture based on magnetic cell levitation.* Nature nanotechnology, 2010. **5**(4): p. 291-296.
14. Jakab, K., et al., *Tissue engineering by self-assembly of cells printed into topologically defined structures.* Tissue Engineering Part A, 2008. **14**(3): p. 413-421.
15. Visconti, R.P., et al., *Towards organ printing: engineering an intra-organ branched vascular tree.* Expert opinion on biological therapy, 2010. **10**(3): p. 409-420.
16. Itoh, M., et al., *Scaffold-free tubular tissues created by a bio-3D printer undergo remodeling and endothelialization when implanted in rat aortae.* PloS one, 2015. **10**(9): p. e0136681.
17. Yurie, H., et al., *The efficacy of a scaffold-free Bio 3D conduit developed from human fibroblasts on peripheral nerve regeneration in a rat sciatic nerve model.* PloS one, 2017. **12**(2): p. e0171448.
18. Machino, R., et al., *Scaffold-free trachea tissue engineering using bioprinting,* in *C109. Matrix mania: the complex webs we weave?* 2015, Am Thoracic Soc. p. A5343-A5343.
19. Yamamoto, T., et al., *Human urethra-engineered with human mesenchymal stem cell with maturation by rearrangement of cells for self-organization-Newly*

developed scaffold-free three-dimensional bio-printer. The Journal of Urology, 2015. **193**(4): p. e221-e222.
20. Glazier, J.A. and F. Graner, *Simulation of the differential adhesion driven rearrangement of biological cells.* Physical Review E, 1993. **47**(3): p. 2128.
21. Flenner, E., et al., *Kinetic Monte Carlo and cellular particle dynamics simulations of multicellular systems.* Physical Review E, 2012. **85**(3): p. 031907.
22. Graner, F. and J.A. Glazier, *Simulation of biological cell sorting using a two-dimensional extended Potts model.* Physical review letters, 1992. **69**(13): p. 2013.
23. Andréa Dernowsek, J.d., R.A. Rezende, and J.V. Lopes da Silva, *The role of information technology in the future of 3D biofabrication.* Journal of 3D printing in medicine, 2017. **1**(1): p. 63-74.
24. Cristea, A. and A. Neagu, *Shape changes of bioprinted tissue constructs simulated by the Lattice Boltzmann method.* Computers in biology and medicine, 2016. **70**: p. 80-87.
25. Neagu, A., et al., *Computational modeling of tissue self-assembly.* Modern Physics Letters B, 2006. **20**(20): p. 1217-1231.
26. McMurtrey, R.J., *Analytic Models of Oxygen and Nutrient Diffusion, Metabolism Dynamics, and Architecture Optimization in Three-Dimensional Tissue Constructs with Applications and Insights in Cerebral Organoids.* Tissue Engineering Part C: Methods, 2016.
27. Garikipati, K., *Perspectives on the mathematics of biological patterning and morphogenesis.* Journal of the Mechanics and Physics of Solids, 2017. **99**: p. 192-210.
28. Wakao, S., et al., *Morphologic and gene expression criteria for identifying human induced pluripotent stem cells.* PloS one, 2012. **7**(12): p. e48677.
29. Boland, T., et al., *Cell and organ printing 2: Fusion of cell aggregates in three-dimensional gels.* The Anatomical Record Part A: discoveries in molecular, cellular, and evolutionary biology, 2003. **272**(2): p. 497-502.
30. Izaguirre, J.A., et al., *CompuCell, a multi-model framework for simulation of morphogenesis.* Bioinformatics, 2004. **20**(7): p. 1129-1137.
31. Mombach, J.C., et al., *Quantitative comparison between differential adhesion models and cell sorting in the presence and absence of fluctuations.* Physical Review Letters, 1995. **75**(11): p. 2244.
32. Moldovan, N.I., N. Hibino, and K. Nakayama, *Principles of the Kenzan Method for Robotic Cell Spheroid-Based Three-Dimensional Bioprinting.* Tissue Engineering Part B: Reviews, 2017.
33. Sun, Y., X. Yang, and Q. Wang, *In-silico analysis on biofabricating vascular networks using kinetic Monte Carlo simulations.* Biofabrication, 2014. **6**(1): p. 015008.
34. Mueller-Klieser, W. and R. Sutherland, *Oxygen tensions in multicell spheroids of two cell lines.* British journal of cancer, 1982. **45**(2): p. 256.
35. Murphy, K.C., et al., *Measurement of oxygen tension within mesenchymal stem cell spheroids.* Journal of The Royal Society Interface, 2017. **14**(127): p. 20160851.
36. Haji-Karim, M. and J. Carisson, *Proliferation and viability in cellular spheroids of human origin.* Cancer research, 1978. **38**(5): p. 1457-1464.
37. Freyer, J.P. and R.M. Sutherland, *Regulation of growth saturation and development of necrosis in EMT6/Ro multicellular spheroids by the glucose and oxygen supply.* Cancer research, 1986. **46**(7): p. 3504-3512.

38. Macklin, P., et al., *Progress Towards Computational 3-D Multicellular Systems Biology*, in *Systems Biology of Tumor Microenvironment*. 2016, Springer. p. 225-246.
39. Hashem, M., et al., *Electron spin resonance microscopic imaging of oxygen concentration in cancer spheroids.* Journal of Magnetic Resonance, 2015. **256**: p. 77-85.
40. Folkman, J., *Tumor angiogenesis: therapeutic implications.* New england journal of medicine, 1971. **285**(21): p. 1182-1186.
41. Moldovan, N.I., et al., *Reoxygenation-derived toxic reactive oxygen/nitrogen species modulate the contribution of bone marrow progenitor cells to remodeling after myocardial infarction.* Journal of the American Heart Association, 2014. **3**(1): p. e000471.
42. Cook, C.A., et al., *Oxygen delivery from hyperbarically loaded microtanks extends cell viability in anoxic environments.* Biomaterials, 2015. **52**: p. 376-384.
43. Shweiki, D., et al., *Induction of vascular endothelial growth factor expression by hypoxia and by glucose deficiency in multicell spheroids: implications for tumor angiogenesis.* Proceedings of the National Academy of Sciences, 1995. **92**(3): p. 768-772.